Journal of Building Engineering 93 (2024) 109867

Contents lists available at ScienceDirect

Journal of Building Engineering

journal homepage: www.elsevier.com/locate/jobe

# Chloride ingress analysis on alkali-activated slag concrete: A validated modelling framework for long-term assessment

Bin Dong [a], Yuguo Yu [b,**], Yuan Feng [a], Jie Yang [c], Gaofeng Zhao [d], Wei Gao [a,*]

[a] Centre for Infrastructure Engineering and Safety, School of Civil and Environmental Engineering, The University of New South Wales, Sydney, NSW, 2052, Australia
[b] Civil & Infrastructure Engineering, School of Engineering, RMIT University, Melbourne, Victoria, 3000, Australia
[c] School of Engineering, RMIT University, PO Box 71, Bundoora, VIC, 3083, Australia
[d] State Key Laboratory of Hydraulic Engineering Simulation and Safety, School of Civil Engineering, Tianjin University, Tianjin, 300354, China

ARTICLE INFO

*Keywords:*
Alkali-activated slag concrete
Finite element analysis
Gibbs energy minimisation
Hybrid chloride binding modelling
Long-term chloride ingress

ABSTRACT

Amidst global commitment to reduce $CO_2$ emissions, the forthcoming decades expect to witness the prevalence of alkali-activated materials. As a predominant trigger for reinforcement corrosion, the accurate prediction of chloride ingress is paramount for the widespread application of the emerging building material. In this regard, this paper presents a novel framework tailored for analysing long-term chloride penetration into alkali-activated slag (AAS) concrete. An innovative technique for modelling chloride binding is developed and integrated into the framework. The technique can spontaneously assess time-dependent chloride binding based on the detailed phase assemblage, thereby rendering the framework applicability for the long-term analysis. The effectiveness of this model is rigorously validated against experiments. Furthermore, a series of virtual experiments are conducted by using the verified model to investigate the impact of different activators, where the distinction of resulting AAS concretes in resisting chloride ingress is elucidated. Overall, the present model is promising in delivering comprehensive understanding and robust prediction concerning long-term behaviours of next-generation AAS concrete buildings.

## 1. Introduction

The exploration of low-carbon substitutes for ordinary Portland cement (OPC) stands as a pressing pursuit in the building construction industry [1–8], particularly after the conclusion of 2015 Paris Agreement [9]. Alkali-activated slag (AAS), created via chemical reactions between slag and alkaline activators, has gained widespread recognition as an alternative material [10–18]. Notably, compared to conventional OPC concrete, this emerging green building material shows higher resistance to chloride ingress for retarding reinforcement corrosion [19,20]. This advantage positions AAS concrete as a promising choice for structures exposed to chloride-laden environments. As a pivotal factor in retarding chloride-induced corrosion in concrete [21–24], substantial endeavours have been dedicated to understanding chloride binding in AAS concrete to facilitate applications of the material [25–37].

Fig. 1 summarises the observed hydrates with binding capacities in AAS concrete. As shown in Fig. 1, several hydrates have been identified to be capable of physically absorbing chloride, such as calcium (-sodium) aluminosilicate hydrate (C-(N)-A-S-H) and Mg–Al

* Corresponding author.
** Corresponding author.
*E-mail addresses:* yuguo.yu@rmit.edu.au (Y. Yu), w.gao@unsw.edu.au (W. Gao).

https://doi.org/10.1016/j.jobe.2024.109867
Received 20 March 2024; Received in revised form 30 May 2024; Accepted 5 June 2024
Available online 6 June 2024

layered double hydroxide (MgAl–OH-LDH) phases [33–36]. Moreover, despite typically forming in alkali-activated fly ash systems, Myers et al. [37] also detected the precipitation of sodium aluminosilicate hydrate (N-A-S-H) in AAS cements, known for its greater physical binding capacity compared to C-(N)-A-S-H [32]. In addition to physical binding, AAS concrete can chemically bind chloride through the mechanism of ionic exchange [27–31], where the transformation of katoite and AFm phases into Cl-containing Friedel's salt has been substantiated [27–29]. It has also been documented that MgAl–OH-LDH may transform into chloride intercalated hydrotalcite in the presence of chloride, owing to its positively charged layered structure [30,31]. However, Zuo [27] performed a systematic thermodynamic examination and suggested that such a chemical binding mechanism linked to MgAl–OH-LDH does not exhibit under the attack of NaCl solution. The finding aligns with the experimental observation reported by Ke et al. [35].

Despite that a great variety of hydrates have been recognised to possess binding capacities, the existence of these hydrates shows significant inconsistency within different AAS concretes [38–40]. A phase diagram, established in a recent study [41], has disclosed that the presence of specific hydrates in AAS concrete is strongly contingent upon the chemical composition of raw slag and the type of alkaline solution employed for activation. Therefore, AAS concrete tends to manifest distinctive binding capacities in engineering practices [35,42], depending on its specific hydrate composition. During prolonged exposure to environment, the chloride binding capacity of AAS concrete may further be complicated by leaching [43]. Leaching is a common phenomenon frequently observed in concrete structures [44–47], resulting from disparities in ionic concentrations between exposure solution and pore solution. Driven by the concentration gradients, certain ions, such as $Ca^{2+}$ and $OH^{-}$, are inclined to leach out of concrete simultaneously with chloride ingress. The system equilibrium may be disturbed by changes in pore solution composition, leading to gradual dissolution of hydrates near the exposure surface, as depicted in Fig. 1. As a result, the binding capacity of AAS concrete exhibits as a time-dependent material property under long-term service.

Such a complex mechanism of chloride binding imposes notable challenges to the robust analysis of chloride transportation in AAS concrete, which is essential to the comprehension and prediction for the long-term durability performance of buildings. In general, the simplified chloride binding isotherm is the most popular method for evaluating concrete binding capacity, widely utilised in analysing OPC concrete [48–52]. However, a direct application of this approach to AAS concrete is prevented by the complexity of identifying a set of universal binding coefficients for different AAS concretes, owing to the varied phase assemblage and the impact of time-dependent leaching amid long-term exposures. In this regard, the powerful thermodynamic technique may hold great promise to tackle the problem, where a successful implementation has been reported for evaluating the chemical binding of various AAS concretes with premixed chloride [27]. Nevertheless, its further application is limited due to presently inadequate knowledge towards thermodynamically assessing the physical binding mechanism of the novel material. As a result, an approach to reliably evaluate the total chloride binding capacity of AAS concrete has yet been reported, resulting in a lack of a validated model for accurately analysing the long-term chloride penetration process.

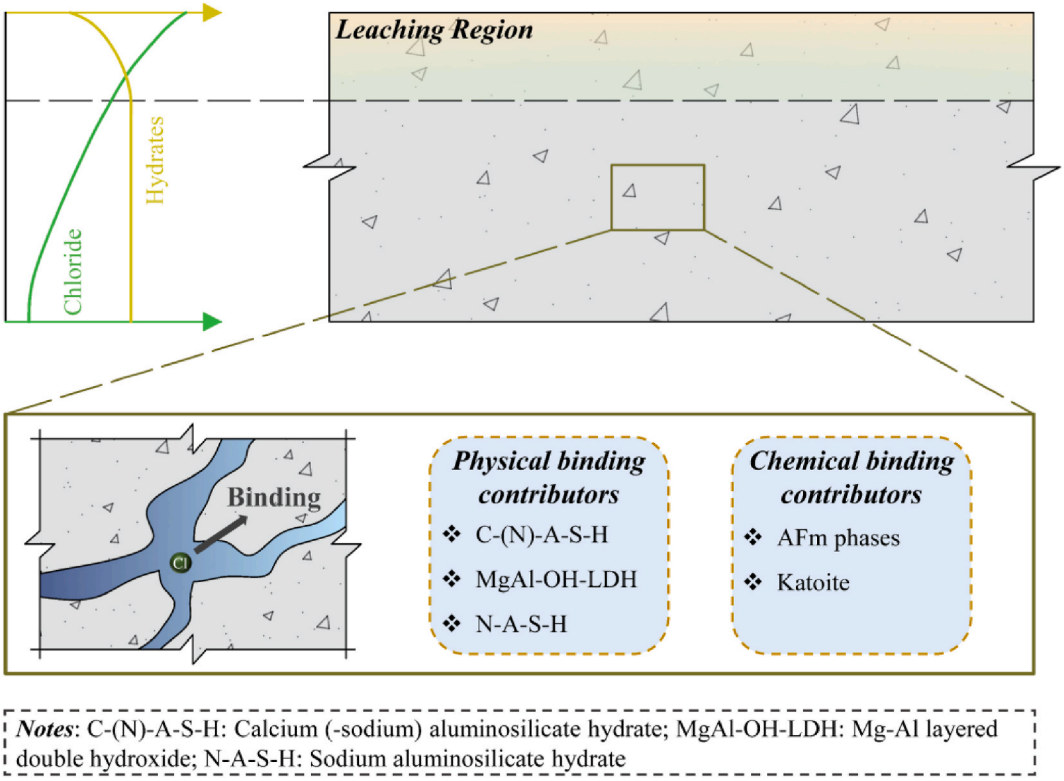


**Fig. 1.** Chloride binding and leaching in AAS concrete during chloride ingress.

To address this outstanding research gap, a numerical framework is freshly developed to investigate the long-term ingress of chloride into AAS concrete, where the major contribution lies in integrating an innovative modelling of chloride binding in AAS concrete. To be more specific, a hybrid modelling technique for chloride binding is developed within the framework by combining the binding isotherm with thermodynamic modelling. By doing so, chloride binding is enabled to be assessed based on available phase assemblage, directly addressing the scientific difficulty arising from varied hydrate composition in different AAS concretes. Moreover, the employed thermodynamic method also facilitates a comprehensive evaluation on the hydrate evolution in the process of chloride ingress, where the time-dependence of binding capacities is automatically captured. As a result, the framework is applicable to AAS concretes in long-term chloride ingress analyses, contributing to the performance-based design and engineering applications of next-generation reinforced AAS concrete buildings.

In the following context, the framework is developed in detail in Section 2, where its effectiveness is carefully investigated in Section 3 against reported experiments. Subsequently, a series of virtual experiments is performed in Section 4 to investigate the influence of different alkaline activators on chloride ingress. Finally, several valuable insights are presented in Section 5.

## 2. Model formulation

As discussed, the transport of chloride in concrete involves intricate interactions with the hydrate system via both physical and chemical binding effects. The complexity is further enhanced by the simultaneous chemical reactions between solid phases and other ionic species, giving rise to a multi-ionic reactive transportation problem. As widely recognised in the literature [53–55], it is intractable to tackle such a complex mechanism through a fully coupled solution strategy. In this regard, this study establishes the numerical framework based on the popular operator splitting approach (OSA) [54], where the fundamental is to split the evaluation of chemical reactions from multi-ionic transportation modelling. Following this principle, the detailed development of the framework is elaborated in this section, with an innovative method for modelling chloride binding in AAS concrete highlighted in Section 2.2.

### 2.1. Modelling multi-ionic transportation

The transportation of ionic species in concrete can be triggered by a variety of mechanisms, including diffusion, electromigration, chemical activity coupling of ions, thermal conduction, and moisture movement. Focusing on saturated and isothermal exposure conditions, the modified Poisson-Nernst-Planck (PNP) model [48,56,57] is adopted to mathematically describe the multi-ionic transportation process in Eqs. (1)–(3), where the effect of physical binding on chloride transportation is specifically considered. Following the OSA solution scheme, the influence of chemical reactions, such as the chemical binding of chloride, on the ionic transportation is omitted from the modified PNP model.

$$w_{\mathrm{L}}\frac{\partial c_i}{\partial t}=\nabla\cdot\left(D_i w_{\mathrm{L}}\nabla c_i+\frac{D_i z_i \mathrm{F}}{\mathrm{R}T}c_i w_{\mathrm{L}}\nabla\varphi+D_i w_{\mathrm{L}} c_i\nabla\ln\gamma_i\right) \tag{1}$$

$$w_{\mathrm{L}}\frac{\partial c_{\mathrm{Cl}}}{\partial t}+\frac{\partial c_{\mathrm{Cl}}^{\mathrm{phy}}}{\partial t}=\nabla\cdot\left(D_{\mathrm{Cl}} w_{\mathrm{L}}\nabla c_{\mathrm{Cl}}+\frac{D_{\mathrm{Cl}} z_{\mathrm{Cl}}\mathrm{F}}{\mathrm{R}T}c_{\mathrm{Cl}} w_{\mathrm{L}}\nabla\varphi+D_{\mathrm{Cl}} w_{\mathrm{L}} c_{\mathrm{Cl}}\nabla\ln\gamma_{\mathrm{Cl}}\right) \tag{2}$$

$$\nabla\cdot(\tau w_{\mathrm{L}}\nabla\varphi)+\frac{\mathrm{F}}{\varepsilon}w_{\mathrm{L}}\sum_i z_i c_i=0 \tag{3}$$

where $c_i$, $D_i$, $z_i$, and $\gamma_i$ are the concentration (mol/m$^3$ of pore solution), diffusion coefficient (m$^2$/s), valence number ($-$), and chemical activity coefficient ($-$) of $i$th ion, respectively, $w_{\mathrm{L}}$ is the liquid volume fraction in concrete (m$^3$/m$^3$ of concrete), F is the Faraday constant (96485.333 C/mol), R is the ideal gas constant (8.3143 J/mol/K), $T$ is temperature (K), $c_{\mathrm{Cl}}^{\mathrm{phy}}$ indicates the physical binding capacity of concrete (mol/m$^3$ of concrete), $\tau$ is the tortuosity of the pore system ($-$).

### 2.2. A hybrid modelling technique for chloride binding in AAS concrete

#### 2.2.1. Modelling physical binding of chloride

As clearly demonstrated in Eq. (2), a key in solving the multi-ionic transportation model lies in assessing the physical binding capacity of concrete. Referring to Fig. 1, the physical binding of chloride in AAS concrete is attributed to a variety of hydrates, including C-(N)-A-S-H, MgAl–OH-LDH and N-A-S-H phases. The assemblage of these phases is subjected to dynamic change under long-term exposure, resulting in a time-dependent physical binding capacity of the concrete. To date, a model to quantitatively assess physically bound chloride in AAS concrete has not been reported in the literature. A recent experimental study conducted by Ke et al. [35] has extensively measured the binding capacity of synthetic C-(N)-A-S-H and MgAl–OH-LDH. The reported data serves as a solid foundation for developing an empirical model to address the research gap. In specific, the present study utilises the popular Langmuir isotherm [58] to describe the binding capacity of individual hydrate, with model parameters calibrated using the data measured by Ke et al. [35], as shown in Eq. (4). By doing so, the extent of physical binding of chloride to AAS concrete can be calculated by Eqs. (5) and (6).

$${}^{j}c_{\mathrm{Cl}}^{\mathrm{phy}}=\frac{\alpha_j c_{\mathrm{Cl}}}{1+\beta_j c_{\mathrm{Cl}}} \tag{4}$$

$$c_{\mathrm{Cl}}^{\mathrm{phy}} = \sum_j \frac{\overline{\alpha}_j c_{\mathrm{Cl}}}{\left(1+\beta_j c_{\mathrm{Cl}}\right)} \tag{5}$$

with

$$\overline{\alpha}_j = \frac{N_j \alpha_j}{k M_{\mathrm{Cl}}} \tag{6}$$

where in Eq. (4), ${}^{j}c_{\mathrm{b}}^{\mathrm{phy}}$ (g/g of hydrate) indicates the amount of chloride that is physically bound to the $j$th hydrate, $\alpha_j$ and $\beta_j$ are binding coefficients related to the $j$th hydrate, where the calibrated values are summarised in Table 1. Owing to the limited information available regarding N-A-S-H, its binding capacity is assumed to be consistent with C-(N)-A-S-H. Given higher binding capacity of N-A-S-H than C-(N)-A-S-H [32], this is a conservative assumption. In Eqs. (5) and (6), $M_{\mathrm{Cl}}$ (35.453 g/mol) is the molar mass of chlorine, $k$ = 3 is the parameter to reflect property difference between synthetic and amorphous hydrates reported by Mundra et al. [42], $N_j$ (g/m$^3$ of concrete) is the time-dependent content of the $j$th hydrate in AAS concrete, which can be evaluated through the chemical reaction analysis in the following section.

The physical binding capacity of AAS concrete as estimated by Eq. (5) is then integrated into Eq. (2) through Eq. (7), yielding the governing equation for chloride transportation in Eq. (8).

$$\frac{\partial c_{\mathrm{Cl}}^{\mathrm{phy}}}{\partial t} = \frac{\partial c_{\mathrm{Cl}}^{\mathrm{phy}}}{\partial c_{\mathrm{Cl}}} \frac{\partial c_{\mathrm{Cl}}}{\partial t} = \left( \sum_j \frac{\overline{\alpha}_j}{\left(1+\beta_j c_{\mathrm{Cl}}\right)^2} \right) \frac{\partial c_{\mathrm{Cl}}}{\partial t} \tag{7}$$

$$\left[ w_{\mathrm{L}} + \sum_j \frac{\overline{\alpha}_j}{\left(1+\beta_j c_{\mathrm{Cl}}\right)^2} \right] \frac{\partial c_{\mathrm{Cl}}}{\partial t} = \nabla \cdot \left( D_{\mathrm{Cl}} w_{\mathrm{L}} \nabla c_{\mathrm{Cl}} + \frac{D_{\mathrm{Cl}} z_{\mathrm{Cl}} \mathrm{F}}{\mathrm{R}T} c_{\mathrm{Cl}} w_{\mathrm{L}} \nabla \varphi + D_{\mathrm{Cl}} w_{\mathrm{L}} c_{\mathrm{Cl}} \nabla \ln \gamma_{\mathrm{Cl}} \right) \tag{8}$$

*2.2.2. Modelling chemical binding of chloride and other simultaneous reactions*

With the time-dependent distribution of ionic composition obtained, the chemical system of AAS concrete is investigated by a thermodynamic modelling technique. It enables a comprehensive evaluation into the chemical chloride binding, wherein several phases may undergo transformation into Friedel's salt. Notably, the thermodynamic analysis also encompasses other concurrent chemical processes, with particular emphasis on the dissolution of certain hydrates triggered by leaching. By doing so, the evolution of hydrates contributing to both chemical and physical chloride binding can be accurately assessed, thereby capturing the time-dependence of the binding phenomena.

In the present study, a well-established thermodynamic approach, namely Gibbs energy minimisation (GEM) method [59,60], is exploited. The effectiveness of this approach in addressing chemistry-related problems involved in cementitious materials has widely been acknowledged [61,62], and applications in AAS concrete have been reported in [27,63–65]. The basic physicochemical principle of the modelling technique is presented in Eqs. (9) and (10).

$$\min_{\boldsymbol{n}} G = \boldsymbol{n}^{\mathrm{T}} \boldsymbol{u} \quad \text{subject to} \begin{cases} \boldsymbol{W}\boldsymbol{n} = \boldsymbol{b} \\ \boldsymbol{n} \geq \boldsymbol{0} \end{cases} \tag{9}$$

$$\boldsymbol{u} = \boldsymbol{u}^{\circ} + RT \ln \boldsymbol{a} \tag{10}$$

where in Eq. (9), $G$ is the total Gibbs energy of the chemical system in AAS concrete (kJ), $\boldsymbol{n}$ is the vector constructed by molar amounts of species in the chemical system (mol), $\boldsymbol{u}$ is the vector of the chemical potentials of species (kJ/mol), $\boldsymbol{W}$ is the formula matrix of species ($-$), $\boldsymbol{b}$ is the prescribed molar amount of chemical elements (mol). In Eq. (10), $\boldsymbol{u}^{\circ}$ is the vector containing the standard chemical potentials of species, $\boldsymbol{a}$ is the activity vector.

Generally, the effectiveness of thermodynamic modelling relies on the accurate definition of studied chemical system. Herein, the chemical system in AAS concrete is mainly established based on the prevalent Cemdata18 database [66], where thermodynamic properties of typical hydrates observed in experiments are provided. To assess the chemical binding effect, katoite, diverse AFm phases and Friedel's salt are encompassed in the system. Additionally, C-(N)-A-S-H and MgAl–OH-LDH phases are also considered to account for the effect of complicated chemical reactions on the physical binding of chloride, where both phases are modelled as solid solutions. As another phase with physical binding capacity, i.e., N-A-S-H phase, the relevant thermodynamic information has not been reported in the literature. In this regard, the introduction of natrolite to represent N-A-S-H, proven effective in previous studies [27,64], is adopted in this study. Beyond these phases directly linked to chloride binding, the hydrate system is completed with additional solid phases as detected in AAS concrete [41,65], including ettringite, gypsum, magnesium silicate hydrate (M-S-H), brucite, and

**Table 1**
Binding coefficients of hydrates in AAS concrete (in $10^{-5}$).

| | C-(N)-A-S-H & N-A-S-H | MgAl–OH-LDH |
|---|---|---|
| $\alpha$ | 6.145 | 109.7 |
| $\beta$ | − 92.66 | 238.5 |

Ca-heulandite. The thermodynamic information of hydrates used in the chemical analysis is summarised in Appendix A.

After successfully resolving the chemical system, the time-dependent phase assemblage in AAS concrete is obtained. According to the formation of Friedel's salt, Eq. (11) allows for estimating the quantity of chemically bound chloride. Moreover, the precipitation and dissolution of hydrates due to various chemical reactions tend to alter concrete porosity, thereby influencing material diffusivity. In the present study, porosity change is evaluated by Eq. (12), and its impact on diffusion coefficients of ions is considered by the modified Kozeny-Carmon relationship presented in Eq. (13) [49].

$$c_{\mathrm{Cl}}^{\mathrm{che}} = 2 \times \frac{N_{\mathrm{friedel}}}{M_{\mathrm{friedel}}} \tag{11}$$

$$\varphi = \varphi_0 - \Delta V_{\mathrm{S}} \tag{12}$$

$$H_D^{\varphi}(\varphi) = \left(\frac{\varphi}{\varphi_0}\right)^3 \left(\frac{1-\varphi_0}{1-\varphi}\right)^2 \tag{13}$$

where in Eq. (11), $c_{\mathrm{Cl}}^{\mathrm{che}}$ is the quantity of chemically bound chloride (mol/m$^3$ of concrete), $N_{\mathrm{friedel}}$ and $M_{\mathrm{friedel}}$ are the content (g/m$^3$ of concrete) and molar mass (561.33 g/mol) of Friedel's salt. In Eqs. (12) and (13), $\varphi_0$ and $\varphi$ are concrete porosity ( – ) at initial and current states, $\Delta V_{\mathrm{S}}$ is total volumetric change ( – ) due to changes of solid phases, and $H_D^{\varphi}(\varphi)$ is the porosity-related diffusivity multiplier ( – ).

### 2.3. Numerical framework

Thus far, a modelling framework for analysing long-term chloride penetration into AAS concrete has been developed by incorporating a hybrid methodology for assessing the chloride binding capacity. This hybrid approach entails the evaluation of the physical binding of chloride via a binding isotherm, alongside with holistic investigation of chemical binding through thermodynamic analyses. Upon a thorough examination of Eq. (5) and Eq. (9), it is noted that the novel approach directly addresses physical and chemical binding problems based on hydrate assemblage. By doing so, the chloride binding effect in different AAS concretes is able to be captured. Furthermore, given the detailed thermodynamic analyses on varying phase assemblage under enduring exposure, the proposed framework is enabled to deal with the long-term chloride ingress problem in different AAS concretes. The procedure of applying the numerical framework is illustrated in Fig. 2.

According to Fig. 2, the complex chloride ingress problem is decoupled and addressed via a stepwise solution algorithm. To be more specific, this algorithm involves an initial analysis of the multi-ionic transportation within each time step, where the physical binding of chloride is considered by a hydrate-based binding isotherm and integrated into the governing equations. Subsequently, a thermodynamic modelling technique is employed to assess chemical reactions triggered by the transport of ionic species. This approach facilitates solutions of the chemical binding of chloride alongside with other simultaneous chemical reactions. Furthermore, the time-dependent phase assemblage and porosity distribution are updated for the subsequent time step of multi-ionic transportation analysis, where the physical binding capacity towards chloride is also updated according to relevant hydrate contents.

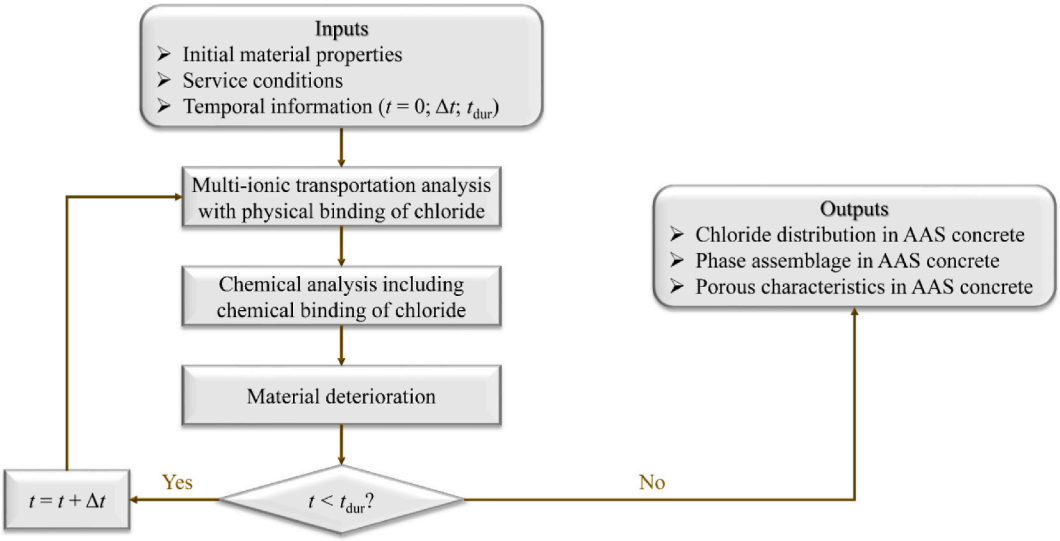


**Fig. 2.** The developed numerical framework for analysing chloride transportation in AAS concrete.

## 3. Numerical validations

### 3.1. Problem statements and numerical setups

In the section, the effectiveness of the developed framework is thoroughly investigated through a careful comparison with two experiments reported by Jiang et al. [67] and Zhang et al. [68]. The experimental configurations are illustrated in Fig. 3, accompanied by a concise description presented as follows.

Jiang et al. [67] casted a rectangular AAS mortar sample by activating fine ground slag powder with sodium silicate nonahydrate. After standard curing, the sample was exposed to 0.5 mol/L NaCl solution for a total of 180 days. To ensure unidirectional penetration of chloride, only one surface of the sample was not sealed with epoxy resin. The content of free chloride was measured along the penetration depth after the exposure of 28, 56, 90 and 180 days.

Zhang et al. [68] constructed a cubic AAS concrete sample using ground granulated blast furnace slag as precursor. The utilised activator contains contents of 6 wt% $SiO_2$ and 4 wt% $Na_2O$ (relative mass to slag), prepared by mixing sodium hydroxide solution, sodium silicate solution and water. Following curing in a chamber, one surface of the sample was subjected to the attack of 3.5 % NaCl solution. The chloride distribution along the penetration direction was measured after the exposure of 90 and 180 days.

According to the detailed mixture design reported in [67], the hydration profiles of both AAS samples are obtained by a GEM-based hydration modelling technique [69]. Due to the lack of a reliable model for assessing hydration kinetics of AAS, the extent of slag reaction is assumed to be 60 %, following the work reported in [27]. Key material properties after hydration are provided in Appendix B, where initial ionic diffusion coefficients are estimated based on the method developed by Samson et al. [54].

In terms of numerical settings of both problems, multi-ionic transportation modelling is implemented in MALAB via an in-house finite element program. The discretisation of domain is achieved using bilinear quadrilateral (Q4) elements, strategically leveraging the inherent symmetry of both problems to substantially diminish the requisite element number. Moreover, the thermodynamic analysis on chemical reactions is also performed within the MATLAB environment. By doing so, the seamless data exchange between two separate steps involved in the OSA solution scheme is realised.

### 3.2. Results and analyses

The evolution of free chloride content (relative weight to concrete) at different depths has been reported in detail by Jiang et al. [67] and Zhang et al. [68]. Through imposing corresponding exposure solution compositions as boundary conditions, numerical results are obtained and compared against experimental measurements in Figs. 4 and 5. Furthermore, chloride distributions without the effect of chloride binding are also modelled for discussions.

According to Figs. 4 and 5, simulated chloride contents consistently align with experimental data over the entire exposure duration in both cases, underscoring the effectiveness of the proposed framework. Moreover, a faster penetration of chloride is commonly observed without the influence of chloride binding. The discrepancy tends to be more pronounced in the later stage of exposure, evidently demonstrating the significance of chloride binding in long-term chloride ingress. To further investigate the important binding phenomena, the distributions of physically and chemically bound chloride are numerically evaluated in Figs. 6 and 7.

The binding effects accompanying with chloride ingress are depicted in Figs. 6 and 7, showing a greater amount of bound chloride than free chloride. This observation elucidates the substantial influence of chloride binding observed in Figs. 4 and 5. Interestingly, the contribution of physical and chemical binding exhibits noticeable differences in these two experiments. In the case of Zhang et al. [68], physical binding consistently surpasses chemical binding in concrete core, while such a phenomenon is not found in the case of Jiang et al. [67]. Indeed, this inconsistency is attributed to the different composition of hydrates present in the two concrete samples as shown in Table B1, verifying the authors' claim that different AAS concretes possess divergent binding capacities. Moreover, the time-dependence of chloride binding is also clearly revealed in both cases, especially at the position near the exposure surface. This discovery can be explained by the evolution of phase assemblage showcased in Figs. 8 and 9.

According to Figs. 8 and 9, C-(N)-A-S-H and MgAl–OH-LDH phases tend to deplete near the exposure surface due to leaching,

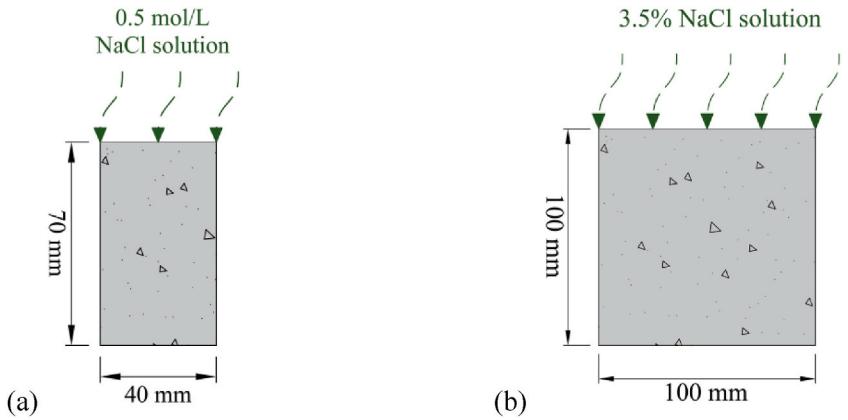


**Fig. 3.** Experimental configurations of: (a) Jiang et al. [67] (b) Zhang et al. [68].

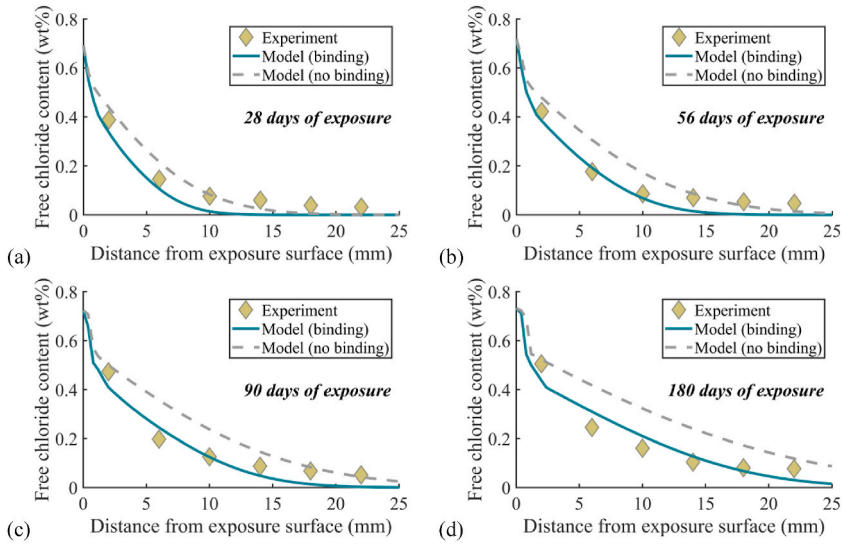


**Fig. 4.** Distribution of free chloride in the case of Jiang et al. [67] at: (a) Day 28; (b) Day 56; (c) Day 90; (d) Day 180.

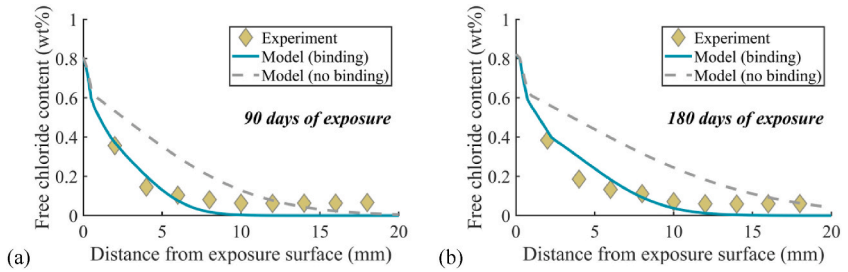


**Fig. 5.** Distribution of free chloride in the case of Zhang et al. [68] at: (a) Day 90; (b) Day 180.

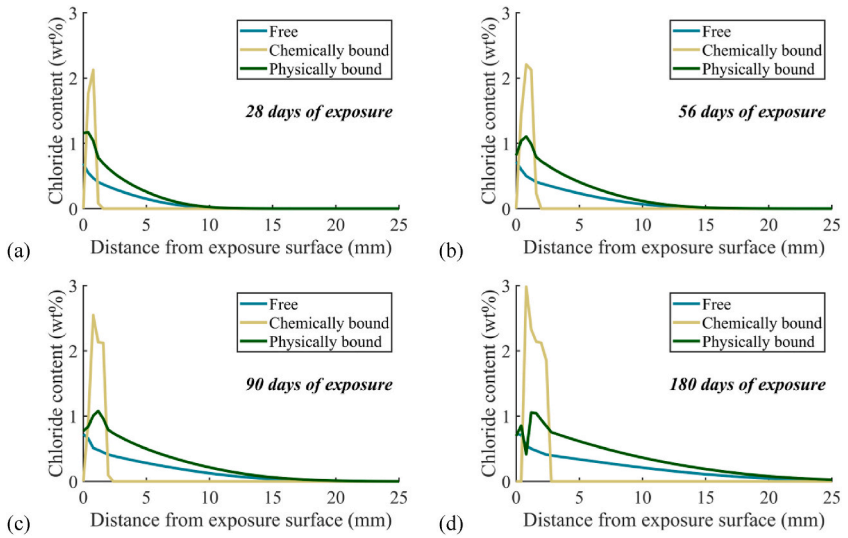


**Fig. 6.** Distribution of bound chloride in the case of Jiang et al. [67] at: (a) Day 28; (b) Day 56; (c) Day 90; (d) Day 180.

inevitably resulting in a weakening of the physical binding capacity of concrete. In comparison to these two phases, another phase with physical binding capacity, i.e., natrolite, demonstrates more intricate behaviours. The complex change of natrolite closely associates with the dissolution of C-(N)-A-S-H. To be more specific, ions released from the dissolved C-(N)-A-S-H can react with abundant $Na^+$

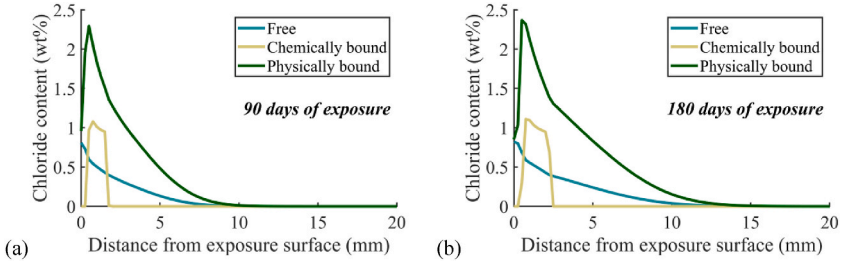


**Fig. 7.** Distribution of bound chloride in the case of Zhang et al. [68] at: (a) Day 90; (b) Day 180.

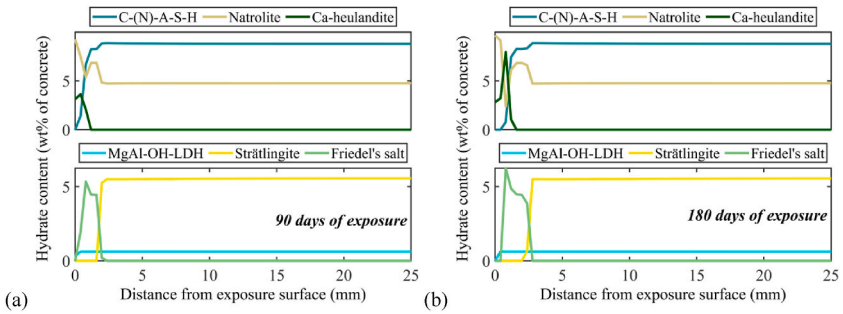


**Fig. 8.** Phase assemblage in AAS concrete produced by Jiang et al. [67] at: (a) Day 90; (b) Day 180.

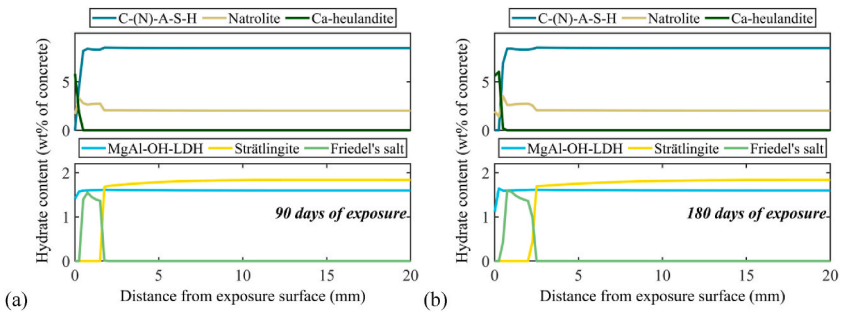


**Fig. 9.** Phase assemblage in AAS concrete produced by Zhang et al. [68] at: (a) Day 90; (b) Day 180.

from external NaCl solution to form natrolite in the region with trace amount of $Ca^{2+}$. The mechanism bears resemblance to the experimentally observed precipitation of N-A-S-H in AAS with low-Ca slag [65]. Moreover, as indicated in Figs. 8 and 9, Ca-heulandite also appears to be thermodynamically stable in the leaching region, competing with the formation of natrolite. Consequently, the precipitation of both natrolite and Ca-heulandite shows complex fluctuations near the exposure surface.

In addition to physical binding, Figs. 8 and 9 also illustrates the pivotal role played by leaching in the chemical binding of chloride. Attributed to leaching, chemically bound chloride in Friedel's salt is released near the exposure surface, representing the

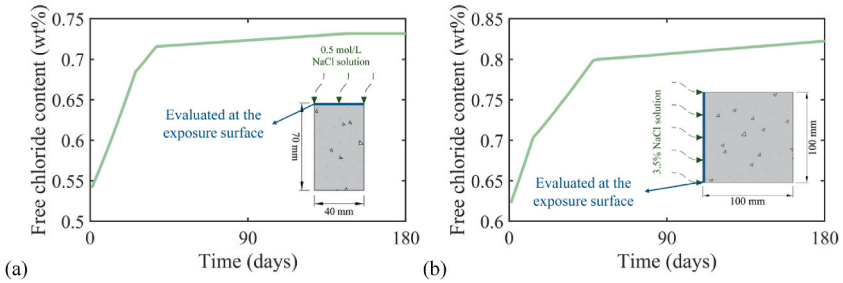


**Fig. 10.** Evolution of free chloride content at the exposure surface in the case of: (a) Jiang et al. [67]; (b) Zhang et al. [68].

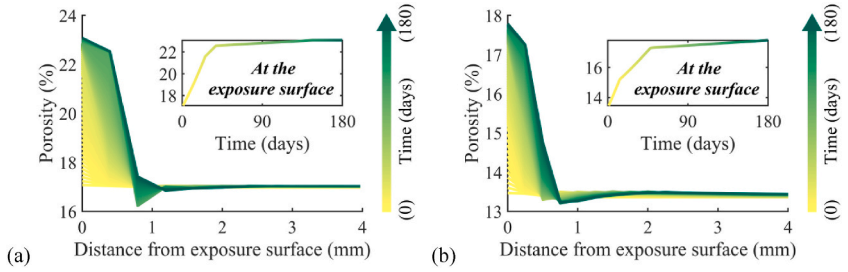


**Fig. 11.** Evolution of porosity distribution in the case of: (a) Jiang et al. [67]; (b) Zhang et al. [68].

**Table 2**
Main chemical composition of slag employed in virtual experiments (wt%) [64].

| CaO | $SiO_2$ | $Al_2O_3$ | MgO | $SO_3$ |
|---|---|---|---|---|
| 42.3 | 32.2 | 13.3 | 5.2 | 2.5 |

**Table 3**
Mix design of AAS concretes prepared by different activators.

| Slag (kg/m$^3$) | $Na_2O$%[a] | Sand (kg/m$^3$) | CA[b] (kg/m$^3$) | w/b[c] | s/a[d] |
|---|---|---|---|---|---|
| 400 | 4 % | 720.3 | 1080.4 | 0.45 | 0.4 |

[a] $Na_2O$% = The equivalent activator dose in terms of $Na_2O$.
[b] CA = Coarse aggregate.
[c] w/b = Water to binder (total mass of slag and solid activator) ratio.
[d] s/a = Sand to aggregate ratio.

disappearance of the chemical binding capacity of concrete. Another intriguing finding in Figs. 8 and 9 is that the formation of Friedel's salt only takes place in a limited region near the exposure surface. Correspondingly, Figs. 6 and 7 reveal the inconsistent distribution ranges occupied by chemically bound chloride and free chloride along the chloride penetration path. This phenomenon can be explained by the thermodynamic theory, stating the fact that the supersaturation state of pore solution is the prerequisite for the precipitation of a solid phase [70]. In this regard, there is a chloride threshold existing to cause the deposition of Friedel's salt and activate the chemical binding effect in theory, which has been confirmed by an experimental observation in AAS binders [28]. Therefore, the chemical binding is not discovered in the deeper layer of concrete core, due to insufficient chloride accumulation.

Upon further investigation on chloride distribution profiles illustrated in Figs. 4 and 5, it is also discovered that the free chloride content experiences a temporal rise at the exposure surface, as examined in Fig. 10. Given the constant chloride concentration in the exposure solution, it is thus speculated that the phenomenon is attributed to the variation in concrete porosity. In this regard, the porosity of both AAS concrete samples during the long-term exposure is analysed and presented in Fig. 11. A gradual increase in porosity at the exposure surface is discovered in Fig. 11, supporting the authors' above assertion. Indeed, the enlarged porosity corresponds to the dissolution of hydrates shown in Figs. 8 and 9, thereby demonstrating another influence of leaching on long-term chloride ingress. Overall, it is thoroughly demonstrated that the present framework is capable of reliably revealing complicated behaviours of diverse AAS concretes in the process of long-term chloride ingress, highlighting the adaptivity of the framework.

## 4. Numerical investigations

It has been widely acknowledged that AAS concretes produced by different activators have distinct hydrate systems [41] and exhibit different chloride binding mechanisms [28]. Herein, a series of virtual experiments are designed and performed by the validated modelling system to investigate the penetration of chloride into AAS concrete prepared with various activators, with the focus on discussing the significant effects of chloride binding capacity in different hydrate systems.

### *4.1. Material design and initial property*

In this study, common sodium-based activators are employed for concrete production [64], encompassing sodium hydroxide (NaOH), sodium metasilicate ($Na_2SiO_3$) and sodium sulfate ($Na_2SO_4$). For simplification, AAS concretes prepared by these activators will be denoted as NH-AAS, NS-AAS, and Ns-AAS in following discussions. Notably, as a type of industrial waste, the chemical composition of slags generally varies from source to source. The investigation on the influence of different slag compositions falls out the scope of current study. In this regard, a conventional European slag reported in [64] is exploited, where its main chemical composition is listed in Table 2.

It is observed in several experimental studies [71,72] that the usage of activator with an equivalent dose of 4 wt% $Na_2O$ contributes to attain desirable early strength of AAS concrete. Therefore, an activator dose with 4 wt% $Na_2O$ is adopted in this study. The detailed mix design for all AAS concretes follows the experimental protocol outlined by Zhang et al. [68], as listed in Table 3. According to [68],

**Table 4**
Initial diffusion coefficients of ions in virtual experiments ( $\times 10^{-12} m^2/s$).

| $OH^-$ | $Na^+$ | $HS^-$ | $Ca^{2+}$ | $SO_4^{2-}$ | $Al(OH)_4^-$ | $H_2SiO_4^{2-}$ | $Mg^{2+}$ | $Cl^-$ |
|---|---|---|---|---|---|---|---|---|
| 9.587 | 2.426 | 3.146 | 1.440 | 1.936 | 1.020 | 1.320 | 1.282 | 3.695 |

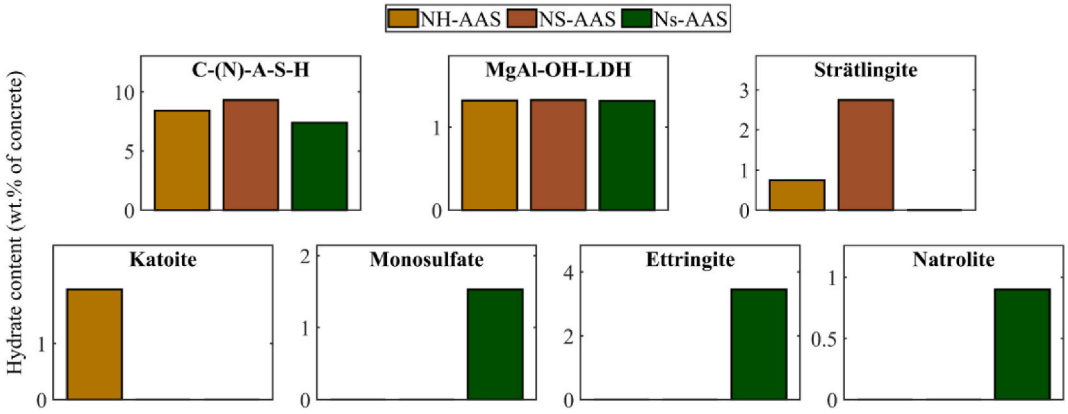


**Fig. 12.** Initial composition of hydrates in AAS concretes prepared by different activators.

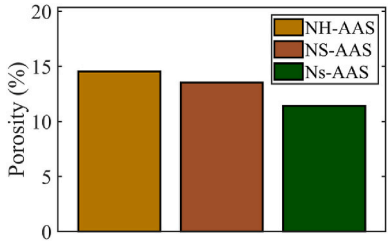


**Fig. 13.** Initial porosity of AAS concretes prepared by different activators.

concrete is casted into cube moulds with size of 100mm × 100mm × 100mm following the mixing. After curing at 20°C for 24 h, the samples are further cured in a curing chamber with relative humidity of 95 % and temperature of 20°C ± 2°C before being subjected to chloride attack.

The initial ionic diffusivity across all samples is assumed to be identical, thus chloride transportation in this investigation is primarily governed by the chemical binding capacity and porosity of the materials. The initial diffusion coefficients of ions utilised in the investigation are summarised in Table 4. To obtain initial hydrate information, the GEM-based hydration modelling technique [69], as utilised in Section 3, is leveraged. The results of the hydration analysis are presented in Figs. 12 and 13, illustrating the initial hydrate system and corresponding porosity for all AAS concretes.

Fig. 12 elucidates the evident impact of activators on the initial hydrate system of the concrete samples. Recognised as the primary reaction product [27], there exists significant variability in the abundance of C-(N)-A-S-H within these AAS concretes. The smallest amount of this hydrate is observed in Ns-AAS, primarily owing to the precipitation of ettringite and monosulfate. The stabilisation of these two products consumes calcium, thereby suppressing the precipitation of C-(N)-A-S-H while promoting the formation of natrolite [41]. Furthermore, instead of monosulfate, the main AFm phase presented in NH-AAS and NS-AAS is strätlingite. However, only a trace amount of strätlingite is found in NH-AAS due to the formation of katoite. These distinct hydrate compositions in AAS concretes contribute to varying porosities, as depicted in Fig. 13. Notably, Ns-AAS possesses the most compact porous system, due to the voluminous presence of ettringite.

### *4.2. Discussions on effects of activators on chloride transportation*

The produced concrete samples are then immersed in 3.5 % NaCl solution for 180 days to trigger unilateral chloride ingress, consistent with the experiment of Zhang et al. [68]. By imposing the exposure condition as the boundary condition, the chloride ingress process in different AAS concretes is numerically examined and illustrated in Fig. 14.

Fig. 14 provides a clear depiction of chloride ingress over a 180-day exposure period. Interestingly, a consistent observation across all cases is the reduction in chloride penetration speed over time, a trend in line with findings from prior studies on OPC concrete [45]. This behaviour may be attributed to the gradual weakening of the driving force provided by the concentration gradient. Additionally, a gradual increase in surface chloride content is observed in all samples, demonstrating the progressive influence of leaching. To directly compare the long-term chloride resistance provided by different activators, free chloride distributions in concretes are further

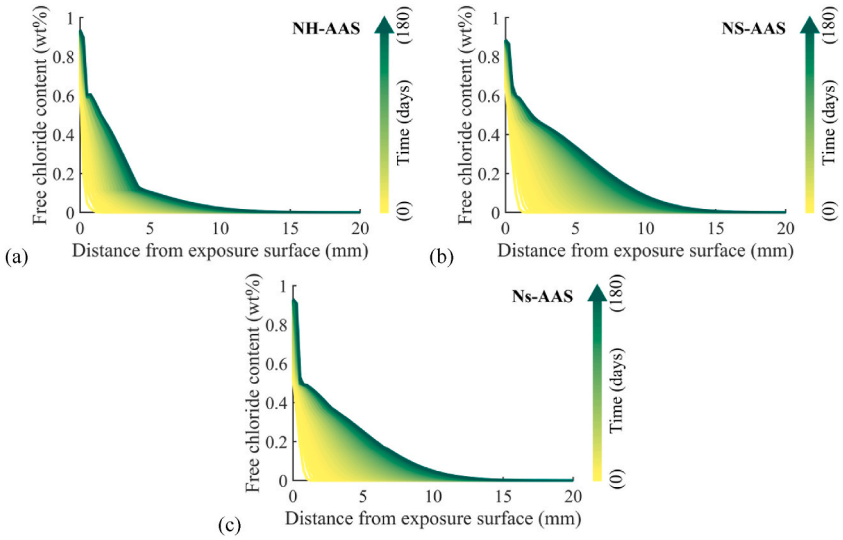


**Fig. 14.** Time-dependent ingress of chloride in: (a) NH-AAS; (b) NS-AAS; (c) Ns-AAS.

evaluated at four time points in Fig. 15.

Despite that smallest porosity is found in Ns-AAS, Fig. 15 illustrates that the material only possesses the smallest chloride content in a thin layer near the exposure surface, with a thickness of approximately 2.5 mm at Day 180. Beyond this layer, the highest resistance to chloride penetration is observed in NH-AAS. After 180 days of exposure, the chloride content at the depth of 5 mm in NH-AAS is less than a half of that in other concretes. As mentioned in Section 4.1, chloride transportation in this study is controlled by chloride binding and porosity. Therefore, it is speculated that the difference in binding capacity among these concretes may be the dominant factor to the observed phenomenon in the deeper layer. To evidence this speculation, the binding capacities of different concretes are further compared. However, their direct comparison based on the quantity of bound chloride is often hindered by the disparate distribution of free chlorides. To tackle this problem, a parameter termed binding factor ($\Re$) is introduced in this study, which is assessed using Eq. (14). Through evaluating the factor, the quantification of binding capacity at a given position $\boldsymbol{x}$ is enabled at a time $t$.

$$\Re_{\mathrm{phy}}(\boldsymbol{x},t)=\frac{c_{\mathrm{Cl}}^{\mathrm{phy}}(\boldsymbol{x},t)}{c_{\mathrm{Cl}}^{\mathrm{free}}(\boldsymbol{x},t)} \tag{14a}$$

$$\Re_{\mathrm{che}}(\boldsymbol{x},t)=\frac{c_{\mathrm{Cl}}^{\mathrm{che}}(\boldsymbol{x},t)}{c_{\mathrm{Cl}}^{\mathrm{free}}(\boldsymbol{x},t)} \tag{14b}$$

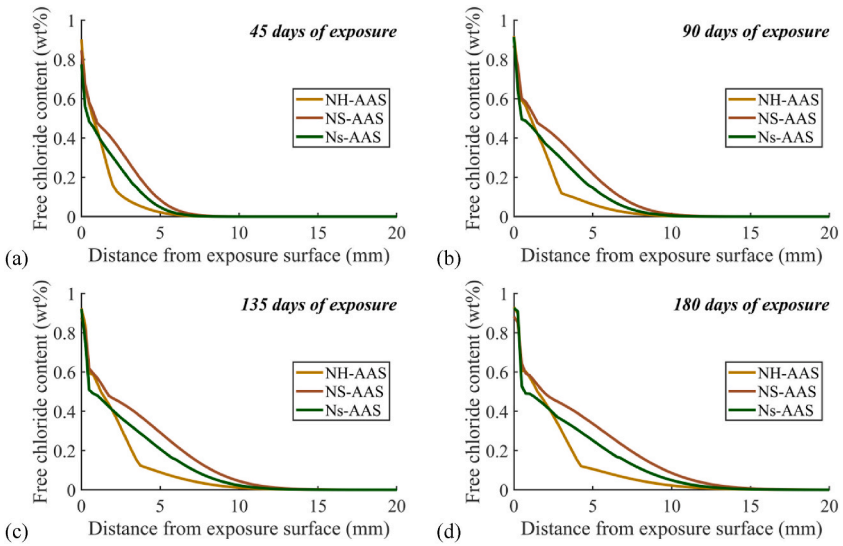


**Fig. 15.** Chloride distribution in AAS concretes at: (a) Day 45; (b) Day 90; (c) Day 135; (d) Day 180.

where $c_{Cl}^{free}$ is the content of free chloride (wt% of concrete), $\Re_{phy}(\boldsymbol{x}, t)$ is the physical binding factor corresponding to physical binding mechanism, $\Re_{che}(\boldsymbol{x}, t)$ is the chemical binding factor for assessing the chemical chloride binding.

Fig. 16 provides an assessment of the physical binding factor at Day 45, Day 90, Day 135, and Day 180. According to Fig. 16, this factor consistently surpasses 2 across all concretes, indicating the significant role played by physical binding in retarding chloride transportation. However, the comparatively small value of the factor observed in NH-AAS does not adequately explain its highest resistance. Consequently, the chemical binding factor is further analysed across all concretes in Fig. 17.

Fig. 17 highlights the substantial disparity in chemical binding factors among different concretes, with NH-AAS consistently showcasing the highest value along the penetration path throughout the exposure period. The chemical binding factor in NH-AAS is found to reach as high as 5, while the value of this factor remains less than 3 in other concretes. This finding indicates that NH-AAS possesses superior chemical binding capacity compared to other materials, notably outperforming Ns-AAS. Moreover, the widest distribution range of the binding factor is also observed in NH-AAS, implying that the chemical binding capacity of the material could be activated in deeper layers of concrete with lesser chloride content. To further investigate this observation, a complementary virtual experiment is conducted. In this virtual experiment, chloride is continuously added to the hydrate system of all concretes. By doing this, the parameter, chloride threshold for chemical binding ($\vartheta_{Cl}$), as proposed in Section 3.2, is enabled to be examined quantitatively. The development of chemical binding resulting from the gradual increment of chloride is presented in Fig. 18, where $\vartheta_{Cl}$ is also compared among all concretes.

Fig. 18 evidently demonstrates the initiation of chemical binding with the gradual addition of chloride. Notably, the chemical binding capacity in NH-AAS allows to be activated with a chloride content below 0.2 %. In contrast, other materials generally require a chloride threshold greater than 0.4 %. Therefore, except for the superior chemical binding capacity, NH-AAS also exhibits the unique characteristics for an easier activation for chemical binding towards chloride. Through the extensive numerical investigations, it is conclusively inferred that the utilisation of NaOH activator remarkably enhances the chemical binding effect in AAS concrete, consequently yielding the greatest resistance to chloride ingress.

## 5. Conclusions

In this paper, a novel modelling framework is developed to investigate the long-term ingress of chloride into AAS concrete. The framework incorporates an innovative technique for modelling chloride binding by integrating binding isotherms of hydrates with a thermodynamic technique. The efficacy of the developed framework is rigorously validated against experimental studies. Subsequently, the numerical system is exploited to probe the influence of activators on the resistance of AAS concrete to chloride ingress, where a binding factor is introduced to quantitatively compare chloride binding capacity of different AAS concretes. Through comprehensive numerical explorations, some valuable insights are gained as follows:

- The binding effects provided by the hydrate system could significantly impede the penetration of chloride into AAS concrete. The contribution of physical and chemical binding, contingent upon the hydrate composition, may significantly vary among different AAS concretes. Consequently, it is imperative to consider and incorporate both binding mechanisms when developing models to robustly predict long-term chloride ingress in AAS concrete.
- Under the effect of leaching, most Ca-rich hydrates tend to diminish near the exposure surface of concrete. This phenomenon can result in a reduction of chloride binding capacity and an increase in porosity, leading to an elevation in surface chloride of about 0.2 % by weight of concrete observed in numerical investigations on reported experiments.

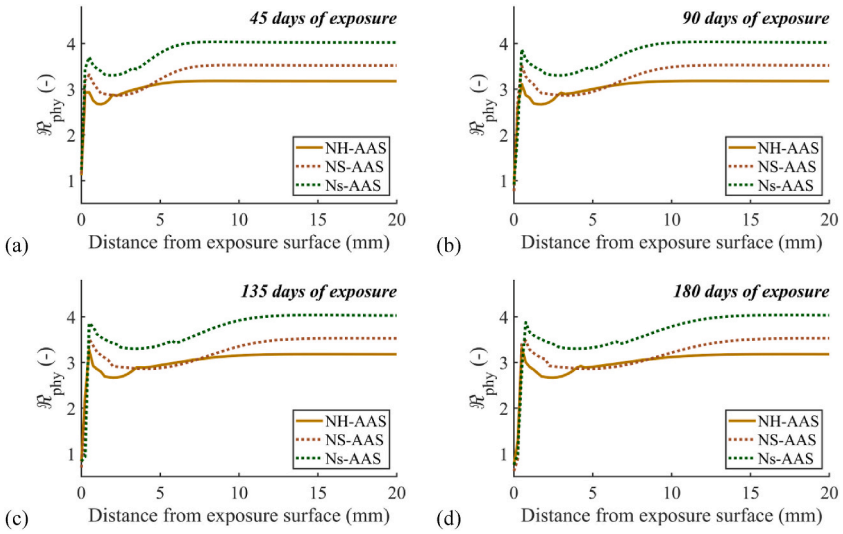


**Fig. 16.** Physical binding factor distribution at: (a) Day 45; (b) Day 90; (c) Day 135; (d) Day 180.

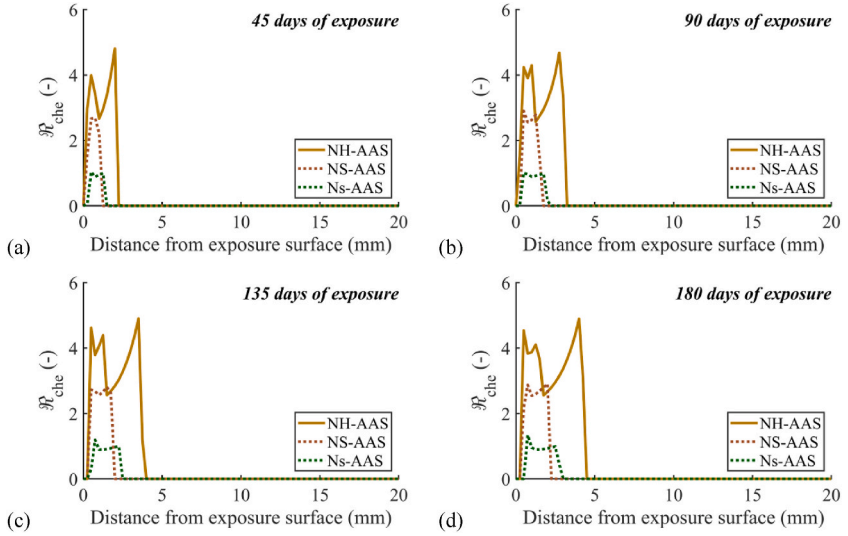


**Fig. 17.** Chemical binding factor distribution at: (a) Day 45; (b) Day 90; (c) Day 135; (d) Day 180.

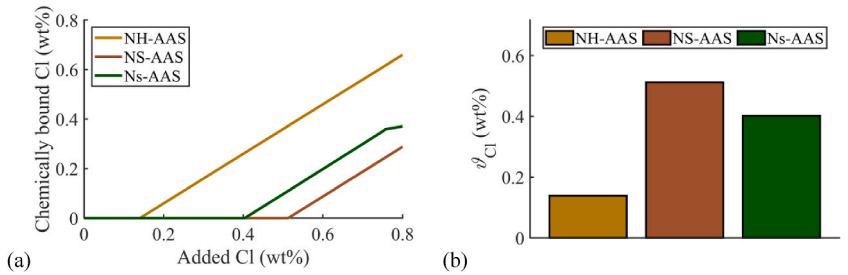


**Fig. 18.** (a) Evolution of chemical binding with the gradual introduction of chloride; (b) chloride threshold for chemical binding ($\vartheta_{Cl}$).

- From a computational perspective, it has been discovered that natrolite/N-A-S-H may precipitate within leaching region with abundant sodium from the external solution. In this region, sodium could combine ions released from the dissolved C-(N)-A-S-H. This finding could serve as an inspiration for subsequent experimental investigations in this domain.
- Following the thermodynamic theory, Friedel's salt is unbale to precipitate within a chemical system until the pore solution attains the required supersaturation state. This implies the presence of a chloride threshold necessary to trigger the chemical binding capacity of hydrates.
- The choice of activator in the production of AAS concrete plays a central role in the penetration of chloride into the material. The utilisation of NaOH triggers not only the greatest chemical binding capacity but also the easiest activation for such a beneficial effect, leading to the highest resistance to chloride penetration observed in numerical exploration. Through implementing the verified model, the chemical binding factor of the AAS concrete prepared by using NaOH activator reaches as high as 5, where its chloride threshold for chemical binding is found to be below 0.2 % by weight of concrete.

Note that above activator-related discussions are grounded in a conventional European slag and some common activators. The developed framework will be employed in the following efforts to further elucidate mechanisms controlling long-term chloride ingress into AAS concrete. For instance, the role played by the kind of the crystal water in $Na_2SiO_3$ in the resistance to chloride ingress will be numerically investigated. Overall, the proposed framework is poised to contribute significantly to the understanding of eco-friendly AAS concrete and its broader application in building engineering.

## CRediT authorship contribution statement

**Bin Dong:** Writing – original draft, Validation, Methodology, Formal analysis, Conceptualization. **Yuguo Yu:** Writing – review & editing, Supervision, Methodology. **Yuan Feng:** Writing – review & editing, Supervision. **Jie Yang:** Writing – review & editing, Supervision. **Gaofeng Zhao:** Writing – review & editing, Supervision. **Wei Gao:** Writing – review & editing, Supervision, Funding acquisition.

## Declaration of competing interest

The authors declare that they have no known competing financial interests or personal relationships that could have appeared to influence the work reported in this paper.

## Data availability

Data will be made available on request.

## Acknowledgements

The research work presented in this paper has been supported by Australian Research Council project IH200100010, IH210100048 and DP240102559. The numerical computations are undertaken with the assistance of resources and services from the National Computational Infrastructure, which is supported by the Australian Government. The second author would also like to acknowledge the financial supports of 2024 Career Reignite Funding Program, Sustainable Development Research Grant, and Sustainable Technologies and Systems EIP Platform Activity Funding from RMIT University.

## Appendix A. Thermodynamic database for hydrates in AAS concrete

**Table A1**
Thermodynamic properties of hydrates included within the framework [65,66].

| | $\Delta_f G°$, kJ/mol | $\Delta_f H°$, kJ/mol | $S°$, J/K/mol |
|---|---|---|---|
| **C-(N)-A-S-H (solid solution I)** | | | |
| $C_1S_{3/2}H_{5/2}$ | −2560.00 | −2831.4 | 152.8 |
| $C_1A_{5/32}S_{38/32}H_{53/32}$ | −2342.90 | −2551.3 | 154.5 |
| $C_1N_{5/16}S_{3/2}H_{19/16}$ | −2452.46 | −2642.0 | 185.6 |
| $C_1A_{5/32}N_{11/32}S_{38/32}H_{42/32}$ | −2474.28 | −2666.7 | 198.4 |
| $C_{5/4}S_{5/4}H_{5/2}$ | −2516.90 | −2780.3 | 159.9 |
| $C_{5/4}A_{1/8}S_1H_{13/8}$ | −2292.82 | −2491.3 | 163.1 |
| $C_{5/4}N_{1/4}A_{1/8}S_1H_{11/8}$ | −2381.81 | −2568.7 | 195.0 |
| $C_{3/2}S_1H_{5/2}$ | −2465.40 | −2720.7 | 167.0 |
| **MgAl–OH-LDH (solid solution II)** | | | |
| $M_4AH_{10}$ | −6358.50 | −7160.2 | 548.9 |
| $M_6AH_{12}$ | −8022.90 | −9006.7 | 675.2 |
| $M_8AH_{14}$ | −9687.40 | −10853.3 | 801.5 |
| **Strätlingite (solid solution III)** | | | |
| $C_2ASH_8$ | −5705.15 | −6360.0 | 546.0 |
| $C_2ASH_7$ | −5464.00 | −6066.8 | 487.6 |
| **Ettringite (solid solution IV)** | | | |
| $C_6As_3H_{32}$ | −15205.94 | −17535.0 | 1900.0 |
| $C_6As_3H_{30}$ | −14728.10 | −16950.2 | 1792.4 |
| **M-S-H (solid solution V)** | | | |
| $M_{1.5}S_2H_{2.5}$ | −3218.43 | −3507.5 | 270.0 |
| $M_{1.5}SH_{2.5}$ | −2355.66 | −2594.2 | 216.0 |
| **Natrolite** | | | |
| $NAS_3H_2$ | −5325.70 | −5728.0 | 360.0 |
| **Katoite** | | | |
| $C_3AH_6$ | −5008.20 | −5537.3 | 422.0 |
| **Monosulfate** | | | |
| $C_4AsH_{12}$ | −7778.40 | −8758.6 | 791.6 |
| **Friedel's salt** | | | |
| $C_3AClH_{10}$ | −6810.90 | −7604 | 731 |
| **Gypsum** | | | |
| $CsH_2$ | −1797.76 | −2023.4 | 193.8 |
| **Brucite** | | | |
| MH | −832.23 | −923.3 | 63.1 |
| **Ca-heulandite** | | | |
| $C_{0.111}A_{0.111}S_{0.778}H_{0.667}$ | −1090.00 | −1179.0 | 87.1 |

Cement shorthand notation is used: A = $Al_2O_3$; C = CaO; Cl = $CaCl_2$; H = $H_2O$; M = MgO; N = $Na_2O$; S = $SiO_2$; s = $SO_3$; c = $CO_2$.

## Appendix B. Initial material properties used for numerical validations

**Table B1**
Basic information of hydrated AAS-based samples in numerical validations

| | Jiang et al. [67] | | Zhang et al. [68] | |
|---|---|---|---|---|
| $\varphi$ | 16.98 % | | 13.37 % | |
| *Concentration* $c_i$ (mol/m$^3$ of pore solution) *& diffusion coefficient* $D_i$ ($\times 10^{-12}$m$^2$/s) of key ions | | | | |
| | $c_i$ | $D_i$ | $c_i$ | $D_i$ |
| $OH^-$ | 94.706 | 26.365 | 130.225 | 9.587 |
| $Na^+$ | 198.678 | 6.670 | 667.505 | 2.426 |
| $HS^-$ | 102.789 | 8.650 | 534.732 | 3.146 |
| $Ca^{2+}$ | 0.326 | 3.960 | 0.602 | 1.440 |
| $SO_4^{2-}$ | 0.153 | 5.325 | 0.971 | 1.936 |
| $Al(OH)_4$ | 1.448 | 2.805 | 1.705 | 1.020 |
| $H_2SiO_4^{2-}$ | 0.041 | 3.630 | 0.052 | 1.320 |
| $Mg^{2+}$ | 2.393e-6 | 3.525 | 2.584e-6 | 1.282 |
| $Cl^-$ | 0 | 10.160 | 0 | 3.695 |
| *Initial hydrate contents* (wt% of concrete) | | | | |
| C-(N)-A-S-H | 8.79 | | 8.47 | |
| MgAl–OH-LDH | 0.62 | | 1.60 | |
| Strätlingite | 5.54 | | 1.84 | |
| Natrolite | 4.76 | | 2.03 | |

## References


[1] S. Guo, Y. Wu, Z. Jia, X. Qi, W. Wang, Sodium-based activators in alkali- activated materials: Classification and comparison, J. Build. Eng. 70 (2023) 106397, https://doi.org/10.1016/J.JOBE.2023.106397.

[2] F. Hong, S. Yu, D. Hou, Z. Li, H. Sun, P. Wang, M. Wang, Study on the mechanical properties, gelling products and alkalization process of alkali-activated metakaolin: from experiment to molecular dynamics simulation, J. Build. Eng. 79 (2023) 107705, https://doi.org/10.1016/J.JOBE.2023.107705.

[3] T. Li, B. Wang, X. Han, X. Zhang, Y. Xing, C. Fan, Z. Liu, Solidification of MSWI fly ash using sodium-montmorillonite in an alkali-activated cementitious system, J. Build. Eng. 75 (2023) 106979, https://doi.org/10.1016/J.JOBE.2023.106979.

[4] C. Lin, Z. Liu, Y. Gao, Z. Li, J. Zhang, H. Niu, Study on the effect and mechanism of cement-based material retarder on red mud-based hybrid alkali activated cement, J. Build. Eng. 70 (2023) 106353, https://doi.org/10.1016/J.JOBE.2023.106353.

[5] Z. Wang, Q. Yuan, C. Zhou, Z. Lu, Y. Nie, Study on the macro-properties and micro-mechanism of solidification construction and demolition waste residue by alkali-activation technology, J. Build. Eng. 78 (2023) 107544, https://doi.org/10.1016/J.JOBE.2023.107544.

[6] M. Yu, H. Lin, T. Wang, F. Shi, D. Li, Y. Chi, L.y. Li, Experimental and numerical investigation on thermal properties of alkali-activated concrete at elevated temperatures, J. Build. Eng. 74 (2023) 106924, https://doi.org/10.1016/J.JOBE.2023.106924.

[7] Y. Zeng, X. Chen, H. Chu, M.Z. Guo, Y. Xu, H. Zhang, Z. Zhu, L. Jiang, Deterioration of alkali-activated and Portland cement-based mortars under sulfur oxidizing bacteria corrosion, J. Build. Eng. 70 (2023) 106418, https://doi.org/10.1016/J.JOBE.2023.106418.

[8] Y. Yu, B. Dong, A. Liu, J. Fu, W. Gao, Phase field to fracture analysis on engineered cementitious composites under complex stress states, Int. J. Mech. Sci. 261 (2024) 108672, https://doi.org/10.1016/J.IJMECSCI.2023.108672.

[9] O.C. Anika, S.G. Nnabuife, A. Bello, E.R. Okoroafor, B. Kuang, R. Villa, Prospects of low and zero-carbon renewable fuels in 1.5-degree net zero emission actualisation by 2050: a critical review, Carbon Capture Sci. Technol. 5 (2022) 100072, https://doi.org/10.1016/J.CCST.2022.100072.

[10] H. Cheng, P. Chen, S. Cao, Y. Li, Stress–strain model of steel fibre-reinforced alkali-activated slag cementitious material after high-temperature exposure, J. Build. Eng. 79 (2023) 107743, https://doi.org/10.1016/J.JOBE.2023.107743.

[11] Z. Jia, R. Cao, S. Zhang, Y. Gao, C. Chen, Y. Zhang, Revealing the difference between creep behavior of hydration products of Portland cement and alkali-activated slag paste at early age, J. Build. Eng. 77 (2023) 107556, https://doi.org/10.1016/J.JOBE.2023.107556.

[12] Q. Li, Z. Ren, X. Su, P. Li, Bond performance of corroded rebars in sustainable alkali-activated slag-based concrete incorporating steel fibers, J. Build. Eng. 85 (2024) 108689, https://doi.org/10.1016/J.JOBE.2024.108689.

[13] Y. Tian, Q. Yuan, C. Yang, K. Yang, L. Yu, M. Zhang, X. Zhu, Insights into the efficiency loss of naphthalene superplasticizer in alkali-activated slag pastes, J. Build. Eng. 68 (2023) 106176, https://doi.org/10.1016/J.JOBE.2023.106176.

[14] Y. Liu, F. Zhou, Y. Shen, H.J. Hwang, Y. Du, Y. Mao, C. Shi, Shear transfer strength of alkali-activated slag-based concrete, J. Build. Eng. 70 (2023) 106304, https://doi.org/10.1016/J.JOBE.2023.106304.

[15] C. Wang, Z. Jin, G. Liu, W. Dong, B. Pang, X. Ding, Mechanisms of chloride transport in low carbon marine concrete: an alkali-activated slag system with high limestone powder, J. Build. Eng. 72 (2023) 106539, https://doi.org/10.1016/J.JOBE.2023.106539.

[16] M. Criado, J.L. Provis, Alkali activated slag mortars provide high resistance to chloride-induced corrosion of steel, Front. Mater. 5 (2018) 34, https://doi.org/10.3389/fmats.2018.00034.

[17] J. Konarik, J. Bohacova, Review of Practical Applications of Alkali-Activated Systems in Construction, 2018, https://doi.org/10.1088/1757-899X/385/1/012030.

[18] K. Yang, C. Yang, J. Zhang, Q. Pan, L. Yu, Y. Bai, First structural use of site-cast, alkali-activated slag concrete in China, Proc. Instit. Civ. Eng. Struct. Build. 171 (2018) 800–809, https://doi.org/10.1680/jstbu.16.00193.

[19] Q. Ma, S.V. Nanukuttan, P.A.M. Basheer, Y. Bai, C. Yang, Chloride transport and the resulting corrosion of steel bars in alkali activated slag concretes, Mater. Struct. 49 (2016) 3663–3677, https://doi.org/10.1617/s11527-015-0747-7.

[20] P.S. Mangat, O.O. Ojedokun, P. Lambert, Chloride-initiated corrosion in alkali activated reinforced concrete, Cem. Concr. Compos. 115 (2021) 103823, https://doi.org/10.1016/J.CEMCONCOMP.2020.103823.

[21] B. Dong, Y. Yu, Y. Feng, D. Wu, G. Zhao, A. Liu, W. Gao, Robust numerical solution for assessing corrosion of reinforced concrete structures under external power supply, Eng. Struct. 294 (2023) 116724, https://doi.org/10.1016/j.engstruct.2023.116724.

[22] B. Dong, Y. Yu, W. Gao, G. Zhao, A novel method for chloride-induced corrosion analysis incorporating consistent ionic diffusivity and concrete resistivity, Construct. Build. Mater. 365 (2023) 129941, https://doi.org/10.1016/J.CONBUILDMAT.2022.129941.

[23] Y. Yu, B. Dong, W. Gao, A. Sofi, Physics-based stochastic aging corrosion analysis assisted by machine learning, Probabilist. Eng. Mech. 69 (2022) 103270, https://doi.org/10.1016/J.PROBENGMECH.2022.103270.
[24] R. Loser, B. Lothenbach, A. Leemann, M. Tuchschmid, Chloride resistance of concrete and its binding capacity–Comparison between experimental results and thermodynamic modeling, Cem. Concr. Compos. 32 (2010) 34–42, https://doi.org/10.1016/j.cemconcomp.2009.08.001.
[25] X. Fan, Y. Wang, Q. Yu, X. Gao, J. Ye, Y. Zhang, Improving the chloride binding capacity of alkali activated slag by calcium and aluminum enriched minerals, J. Build. Eng. 70 (2023) 106384, https://doi.org/10.1016/J.JOBE.2023.106384.
[26] Y. Jun, T. Kim, J.H. Kim, Chloride-bearing characteristics of alkali-activated slag mixed with seawater: effect of different salinity levels, Cem. Concr. Compos. 112 (2020) 103680, https://doi.org/10.1016/J.CEMCONCOMP.2020.103680.
[27] Y. Zuo, Effect of chloride salt on the phase evolution in alkali-activated slag cements through thermodynamic modelling, Appl. Geochem. 136 (2022) 105169, https://doi.org/10.1016/J.APGEOCHEM.2021.105169.
[28] H. Ye, L. Huang, Z. Chen, Influence of activator composition on the chloride binding capacity of alkali-activated slag, Cem. Concr. Compos. 104 (2019) 103368, https://doi.org/10.1016/J.CEMCONCOMP.2019.103368.
[29] J. Zhang, C. Shi, Z. Zhang, Chloride binding of alkali-activated slag/fly ash cements, Construct. Build. Mater. 226 (2019) 21–31, https://doi.org/10.1016/j.conbuildmat.2019.07.281.
[30] X. Ke, S.A. Bernal, O.H. Hussein, J.L. Provis, Chloride binding and mobility in sodium carbonate-activated slag pastes and mortars, Mater. Struct. 50 (2017) 1–13, https://doi.org/10.1617/s11527-017-1121-8.
[31] M.S.H. Khan, O. Kayali, U. Troitzsch, Chloride binding capacity of hydrotalcite and the competition with carbonates in ground granulated blast furnace slag concrete, Mater. Struct. 49 (2016) 4609–4619, https://doi.org/10.1617/s11527-016-0810-z.
[32] N.K. Lee, H.-K. Lee, Influence of the slag content on the chloride and sulfuric acid resistances of alkali-activated fly ash/slag paste, Cem. Concr. Compos. 72 (2016) 168–179, https://doi.org/10.1016/j.cemconcomp.2016.06.004.
[33] I. Ismail, S.A. Bernal, J.L. Provis, R. San Nicolas, D.G. Brice, A.R. Kilcullen, S. Hamdan, J.S.J. van Deventer, Influence of fly ash on the water and chloride permeability of alkali-activated slag mortars and concretes, Construct. Build. Mater. 48 (2013) 1187–1201, https://doi.org/10.1016/j.conbuildmat.2013.07.106.
[34] Y. Zhang, Y. Fang, Y. Shen, Z. Yang, K. Wu, Chloride penetration and binding behavior in unsaturated alkali-activated slag mortars, Cem. Concr. Compos. 140 (2023) 105098, https://doi.org/10.1016/J.CEMCONCOMP.2023.105098.
[35] X. Ke, S.A. Bernal, J.L. Provis, Uptake of chloride and carbonate by Mg-Al and Ca-Al layered double hydroxides in simulated pore solutions of alkali-activated slag cement, Cement Concr. Res. 100 (2017) 1–13, https://doi.org/10.1016/J.CEMCONRES.2017.05.015.
[36] W. Cai, Z. Xu, Z. Zhang, J. Hu, H. Huang, Y. Ma, Z. Zhang, H. Wang, S. Yin, J. Wei, C. Shi, Q. Yu, Chloride binding behavior of synthesized reaction products in alkali-activated slag, Compos. B Eng. 238 (2022) 109919, https://doi.org/10.1016/J.COMPOSITESB.2022.109919.
[37] R.J. Myers, S.A. Bernal, J.D. Gehman, J.S.J. van Deventer, J.L. Provis, The Role of Al in cross-linking of alkali-activated slag cements, J. Am. Ceram. Soc. 98 (2015) 996–1004, https://doi.org/10.1111/jace.13360.
[38] S.A. Bernal, J.L. Provis, R.J. Myers, R. San Nicolas, J.S.J. van Deventer, Role of carbonates in the chemical evolution of sodium carbonate-activated slag binders, Mater. Struct. 48 (2015) 517–529, https://doi.org/10.1617/s11527-014-0412-6.
[39] X. Ke, S.A. Bernal, J.L. Provis, Controlling the reaction kinetics of sodium carbonate-activated slag cements using calcined layered double hydroxides, Cement Concr. Res. 81 (2016) 24–37, https://doi.org/10.1016/j.cemconres.2015.11.012.
[40] S.A. Bernal, R. San Nicolas, R.J. Myers, R.M. de Gutiérrez, F. Puertas, J.S.J. van Deventer, J.L. Provis, MgO content of slag controls phase evolution and structural changes induced by accelerated carbonation in alkali-activated binders, Cement Concr. Res. 57 (2014) 33–43, https://doi.org/10.1016/j.cemconres.2013.12.003.
[41] R.J. Myers, S.A. Bernal, J.L. Provis, Phase diagrams for alkali-activated slag binders, Cement Concr. Res. 95 (2017) 30–38, https://doi.org/10.1016/J.CEMCONRES.2017.02.006.
[42] S. Mundra, D.P. Prentice, S.A. Bernal, J.L. Provis, Modelling chloride transport in alkali-activated slags, Cement Concr. Res. 130 (2020) 106011, https://doi.org/10.1016/J.CEMCONRES.2020.106011.
[43] Z. Chen, H. Ye, Understanding the impact of main seawater ions and leaching on the chloride transport in alkali-activated slag and Portland cement, Cement Concr. Res. 164 (2023) 107063, https://doi.org/10.1016/J.CEMCONRES.2022.107063.
[44] Y. Yu, Y.X. Zhang, A. Khennane, Numerical modelling of degradation of cement-based materials under leaching and external sulfate attack, Comput. Struct. 158 (2015) 1–14, https://doi.org/10.1016/j.compstruc.2015.05.030.
[45] Q.-f. Liu, X.-h. Shen, B. Šavija, Z. Meng, D.C.W. Tsang, S. Sepasgozar, E. Schlangen, Numerical study of interactive ingress of calcium leaching, chloride transport and multi-ions coupling in concrete, Cement Concr. Res. 165 (2023) 107072, https://doi.org/10.1016/j.cemconres.2022.107072.
[46] Y. Yu, W. Gao, A. Castel, A. Liu, X. Chen, M. Liu, Assessing external sulfate attack on thin-shell artificial reef structures under uncertainty, Ocean Eng. 207 (2020) 107397, https://doi.org/10.1016/J.OCEANENG.2020.107397.
[47] Y. Yu, Y.X. Zhang, Effect of capillary connectivity and crack density on the diffusivity of cementitious materials, Int. J. Mech. Sci. 144 (2018) 849–857, https://doi.org/10.1016/J.IJMECSCI.2017.07.058.
[48] Y. Yu, X. Chen, W. Gao, D. Wu, A. Castel, Modelling non-isothermal chloride ingress in unsaturated cement-based materials, Construct. Build. Mater. 217 (2019) 441–455, https://doi.org/10.1016/j.conbuildmat.2019.05.078.
[49] Y. Yu, W. Gao, Y. Feng, A. Castel, X. Chen, A. Liu, On the competitive antagonism effect in combined chloride-sulfate attack: a numerical exploration, Cement Concr. Res. 144 (2021) 106406, https://doi.org/10.1016/J.CEMCONRES.2021.106406.
[50] M. Shafikhani, S.E. Chidiac, A holistic model for cement paste and concrete chloride diffusion coefficient, Cement Concr. Res. 133 (2020) 106049, https://doi.org/10.1016/j.cemconres.2020.106049.
[51] M. Shafikhani, S.E. Chidiac, Quantification of concrete chloride diffusion coefficient–A critical review, Cem. Concr. Compos. 99 (2019) 225–250, https://doi.org/10.1016/j.cemconcomp.2019.03.011.
[52] L.y. Tong, Q. Xiang Xiong, M. Zhang, Z. Meng, F. Meftah, Q.f. Liu, Multi-scale modelling and statistical analysis of heterogeneous characteristics effect on chloride transport properties in concrete, Construct. Build. Mater. 367 (2023) 130096, https://doi.org/10.1016/J.CONBUILDMAT.2022.130096.
[53] E. Samson, J. Marchand, Modeling the effect of temperature on ionic transport in cementitious materials, Cement Concr. Res. 37 (2007) 455–468, https://doi.org/10.1016/j.cemconres.2006.11.008.
[54] E. Samson, J. Marchand, Modeling the transport of ions in unsaturated cement-based materials, Comput. Struct. 85 (2007) 1740–1756, https://doi.org/10.1016/j.compstruc.2007.04.008.
[55] Y. Yu, W. Gao, A. Castel, X. Chen, A. Liu, An integrated framework for modelling time-dependent corrosion propagation in offshore concrete structures, Eng. Struct. 228 (2021) 111482, https://doi.org/10.1016/j.engstruct.2020.111482.
[56] Y. Yu, W. Gao, A. Castel, A. Liu, Y. Feng, X. Chen, A. Mukherjee, Modelling steel corrosion under concrete non-uniformity and structural defects, Cement Concr. Res. 135 (2020) 106109, https://doi.org/10.1016/j.cemconres.2020.106109.
[57] Y. Yu, D. Wu, W. Gao, Stochastic chemo-physical-mechanical degradation analysis on hydrated cement under acidic environments, Appl. Math. Model. 78 (2020) 75–97, https://doi.org/10.1016/j.apm.2019.10.012.
[58] J. Xia, T. Li, J.-X. Fang, W.-l. Jin, Numerical simulation of steel corrosion in chloride contaminated concrete, Construct. Build. Mater. 228 (2019) 116745, https://doi.org/10.1016/j.conbuildmat.2019.116745.
[59] D.A. Kulik, T. Wagner, S.V. Dmytrieva, G. Kosakowski, F.F. Hingerl, K.V. Chudnenko, U.R. Berner, GEM-Selektor geochemical modeling package: revised algorithm and GEMS3K numerical kernel for coupled simulation codes, Comput. Geosci. 17 (2013) 1–24, https://doi.org/10.1007/s10596-012-9310-6.
[60] T. Wagner, D.A. Kulik, F.F. Hingerl, S.V. Dmytrieva, GEM-Selektor geochemical modeling package: TSolMod library and data interface for multicomponent phase models, Can. Mineral. 50 (2012) 1173–1195, https://doi.org/10.3749/canmin.50.5.1173.

[61] B. Lothenbach, G. Le Saout, E. Gallucci, K. Scrivener, Influence of limestone on the hydration of Portland cements, Cement Concr. Res. 38 (2008) 848–860, https://doi.org/10.1016/j.cemconres.2008.01.002.
[62] B. Lothenbach, K. Scrivener, R.D. Hooton, Supplementary cementitious materials, Cement Concr. Res. 41 (2011) 1244–1256, https://doi.org/10.1016/j.cemconres.2010.12.001.
[63] S. Park, B. Lothenbach, J.G. Jang, H.-K. Kim, N. Lee, Thermodynamic modeling and experimental study of carbonation of alkali-activated slag cements, ACS Sustain. Chem. Eng. 11 (2023) 4049–4063, https://doi.org/10.1021/acssuschemeng.2c05789.
[64] X. Ke, S.A. Bernal, J.L. Provis, B. Lothenbach, Thermodynamic modelling of phase evolution in alkali-activated slag cements exposed to carbon dioxide, Cement Concr. Res. 136 (2020) 106158, https://doi.org/10.1016/J.CEMCONRES.2020.106158.
[65] R.J. Myers, B. Lothenbach, S.A. Bernal, J.L. Provis, Thermodynamic modelling of alkali-activated slag cements, Appl. Geochem. 61 (2015) 233–247, https://doi.org/10.1016/J.APGEOCHEM.2015.06.006.
[66] B. Lothenbach, D.A. Kulik, T. Matschei, M. Balonis, L. Baquerizo, B. Dilnesa, G.D. Miron, R.J. Myers, Cemdata18: a chemical thermodynamic database for hydrated Portland cements and alkali-activated materials, Cement Concr. Res. 115 (2019) 472–506, https://doi.org/10.1016/J.CEMCONRES.2018.04.018.
[67] L. Jiang, Y. Niu, W. Jin, H. Gao, L. Chen, Influence of chloride salt type on chloride ion diffusion performance of alkali-activated slag mortar, Construct. Build. Mater. 351 (2022) 128930, https://doi.org/10.1016/J.CONBUILDMAT.2022.128930.
[68] J. Zhang, Y. Ma, J. Zheng, J. Hu, J. Fu, Z. Zhang, H. Wang, Chloride diffusion in alkali-activated fly ash/slag concretes: role of slag content, water/binder ratio, alkali content and sand-aggregate ratio, Construct. Build. Mater. 261 (2020) 119940, https://doi.org/10.1016/J.CONBUILDMAT.2020.119940.
[69] F. Winnefeld, B. Lothenbach, Hydration of calcium sulfoaluminate cements—experimental findings and thermodynamic modelling, Cement Concr. Res. 40 (2010) 1239–1247, https://doi.org/10.1016/j.cemconres.2009.08.014.
[70] M. Balonis, B. Lothenbach, G. Le Saout, F.P. Glasser, Impact of chloride on the mineralogy of hydrated Portland cement systems, Cement Concr. Res. 40 (2010) 1009–1022, https://doi.org/10.1016/j.cemconres.2010.03.002.
[71] N. Li, N. Farzadnia, C. Shi, Microstructural changes in alkali-activated slag mortars induced by accelerated carbonation, Cement Concr. Res. 100 (2017) 214–226, https://doi.org/10.1016/J.CEMCONRES.2017.07.008.
[72] S.A. Bernal, J.L. Provis, B. Walkley, R. San Nicolas, J.D. Gehman, D.G. Brice, A.R. Kilcullen, P. Duxson, J.S.J. van Deventer, Gel nanostructure in alkali-activated binders based on slag and fly ash, and effects of accelerated carbonation, Cement Concr. Res. 53 (2013) 127–144, https://doi.org/10.1016/j.cemconres.2013.06.007.